Hinkkanen, Marko; Luomi, Jorma

Induction motor drives equipped with diode rectifier and small dc-link capacitance

Published in:
IEEE Transactions on Industrial Electronics

DOI:
10.1109/TIE.2007.903959

Published: 04/01/2008

Document Version
Peer-reviewed accepted author manuscript, also known as Final accepted manuscript or Post-print

Please cite the original version:
Hinkkanen, M., & Luomi, J. (2008). Induction motor drives equipped with diode rectifier and small dc-link capacitance. *IEEE Transactions on Industrial Electronics*, *55*(1), 312-320.
https://doi.org/10.1109/TIE.2007.903959

Induction Motor Drives Equipped With Diode Rectifier and Small DC-Link Capacitance

Marko Hinkkanen, *Member, IEEE*, and Jorma Luomi, *Member, IEEE*

***Abstract*—This paper deals with sensorless vector-controlled induction motor drives that are fed by a frequency converter equipped with a diode front-end rectifier. A small DC-link capacitance is used, which makes it possible to replace the electrolytic capacitors with film capacitors. The natural frequency of the DC link is chosen considerably higher than six times the mains frequency but lower than the switching frequency. A recently proposed sensorless controller can be exploited; only minor modifications for small capacitances are needed. Simulation and experimental results of a 2.2-kW drive equipped with a capacitance of only 24 µF demonstrate operation in a wide speed range.**

***Index Terms*—Control, DC link, film capacitors, sensorless.**

I. Introduction

Frequency converters used in induction motor drives are usually equipped with a cost-effective six-pulse diode rectifier, a voltage-stiff DC link, and a pulse-width-modulated (PWM) inverter. Conventionally, the DC link consists of electrolytic capacitors and a DC choke (or an ac choke at the input of the rectifier). The natural frequency of the DC link is much lower than six-times the mains frequency, resulting in a stiff DC-link voltage. Electrolytic capacitors have a large capacitance per volume. There is an increasing interest in replacing these capacitors by film capacitors having a longer lifetime and no explosion risks, but the DC-link capacitance has to be considerably reduced in order to conserve the size of the capacitor bank.

Small DC-link capacitances have been applied in drives equipped with active rectifiers [1], [2], where both the rectifier and the inverter can be used to control the power balance of the DC link. Commercial drives equipped with a diode rectifier and a small DC-link capacitance are available [3]; a small capacitance is advertised to reduce the mains harmonics, while the dynamic performance of the drive has not been used as an argument. In research publications, the concept of a diode rectifier and a small DC-link capacitance has received little attention, with the exception of recent studies from the viewpoint of pulse-width modulation [4], [5].

In this paper, the dimensioning of the DC link is based on a natural frequency that is higher than six times the mains frequency but lower than the switching frequency. In practice, the mains inductance is sufficient, and no additional choke is needed. The vector control with rotor flux orientation is used. The effects of the small DC-link capacitance on the control system design and control performance are studied. The ripple in the DC-link voltage, especially at six times the mains frequency, is considerably higher than usually. At low speeds, this ripple does not deteriorate the performance, since the duty cycles of the pulse-width modulator are calculated based on the measured DC-link voltage. At high speeds, the flux level is controlled based on the pulsating DC-link voltage in order to maximize the torque [6], [7]. To avoid a braking resistor, the braking scheme proposed in [7] is exploited. Furthermore, restrictions on the dynamics may be needed to prevent an overvoltage in the DC link, except in the case of low-power drives.

The preliminary version of this paper was presented at The 31st Annual Conference of the IEEE Industrial Electronics Society (IECON'05), Raleigh, NC, Nov. 6–10, 2005.

II. System Model

A. Diode Rectifier and DC Link

The models of the drive system components are presented in the following. Fig. 1(a) shows a three-phase model of the mains, the diode rectifier, and the DC link. The mains resistance and inductance are denoted by R_g and L_g, respectively, and the DC-link inductance, resistance, and capacitance are L'_d, R'_d, and C_d, respectively. The phase-to-neutral mains voltages are u_ga, u_gb, and u_gc, having the peak value u_g and the angular frequency ω_g. The current at the output of the rectifier is i_di, while the current and voltage at the input of the inverter are i_d and u_d, respectively. The inverter is not shown in the figure. It is modeled by three ideal changeover switches.

The model in Fig. 1(a) is approximated by a simplified model in Fig. 1(b). The ideal rectified voltage is

$$u_\mathrm{di} = \max\{u_\mathrm{ga},\, u_\mathrm{gb},\, u_\mathrm{gc}\} - \min\{u_\mathrm{ga},\, u_\mathrm{gb},\, u_\mathrm{gc}\} \quad (1)$$

or in terms of its harmonic components

$$u_\mathrm{di} = u_\mathrm{dN}\left[1 - \sum_{n=1}^{\infty} \frac{2}{(6n)^2 - 1}\cos(6n\omega_\mathrm{g} t)\right] \quad (2)$$

where the average is $u_\mathrm{dN} = 3\sqrt{3}u_\mathrm{g}/\pi$. The parameters are [8]

$$L_\mathrm{d} = L'_\mathrm{d} + 2L_\mathrm{g}, \quad R_\mathrm{d} = R'_\mathrm{d} + 2R_\mathrm{g} + 3\omega_\mathrm{g}L_\mathrm{g}/\pi \quad (3)$$

where the term $3\omega_\mathrm{g}L_\mathrm{g}/\pi$ corresponds to the non-ohmic voltage drop due to commutation. The differential equations

$$L_\mathrm{d}\frac{\mathrm{d}i_\mathrm{di}}{\mathrm{d}t} = u_\mathrm{di} - u_\mathrm{d} - R_\mathrm{d}i_\mathrm{di}, \quad i_\mathrm{di} \geq 0 \quad (4a)$$

$$C_\mathrm{d}\frac{\mathrm{d}u_\mathrm{d}}{\mathrm{d}t} = i_\mathrm{di} - i_\mathrm{d} \quad (4b)$$

correspond to Fig. 1(b). From (4), the rate of change of the energy stored in the capacitor can be expressed as

$$\frac{C_\mathrm{d}}{2}\frac{\mathrm{d}u_\mathrm{d}^2}{\mathrm{d}t} = \underbrace{u_\mathrm{di}i_\mathrm{di} - R_\mathrm{d}i_\mathrm{di}^2 - \frac{L_\mathrm{d}}{2}\frac{\mathrm{d}i_\mathrm{di}^2}{\mathrm{d}t}}_{p_\mathrm{di}} - p_\mathrm{d} \quad (5)$$

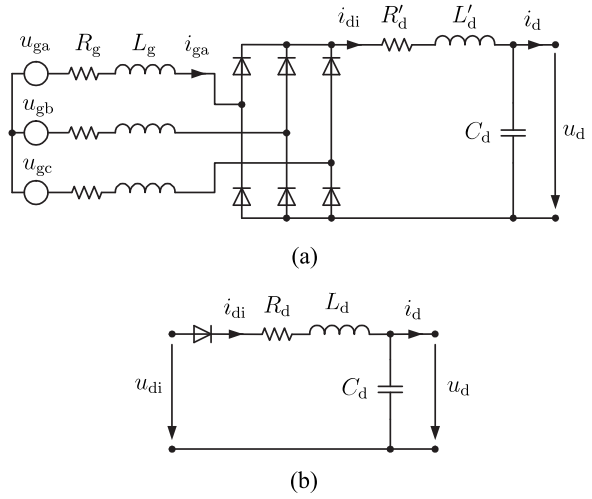

Fig. 1. Mains, diode rectifier, and DC link: (a) typical model; (b) simplified model.

where $p_d = u_d i_d$ is the power into the inverter and $p_{di} = u_d i_{di}$ is the power on the rectifier side of the DC-link capacitance. Advantages of the simplified model in Fig. 1(b) are comparatively short simulation times and easier analysis.

B. Induction Motor and Mechanics

The dynamic model corresponding to the inverse-Γ equivalent circuit [9] of the induction motor will be used. In a general reference frame, the voltage equations are

$$\underline{u}_s = R_s \underline{i}_s + \frac{\mathrm{d}\underline{\psi}_s}{\mathrm{d}t} + \mathrm{j}\omega_k \underline{\psi}_s \tag{6a}$$

$$0 = R_R \underline{i}_R + \frac{\mathrm{d}\underline{\psi}_R}{\mathrm{d}t} + \mathrm{j}\,(\omega_k - \omega_m)\,\underline{\psi}_R \tag{6b}$$

where $\underline{u}_s$ is the space vector of the stator voltage, $\underline{i}_s$ the space vector of the stator current, R_s the stator resistance, and ω_k the electrical angular speed of the reference frame. The rotor resistance is R_R, the rotor current $\underline{i}_R$, and the electrical angular speed of the rotor ω_m. The stator and rotor flux linkages are

$$\underline{\psi}_s = (L'_s + L_M)\,\underline{i}_s + L_M \underline{i}_R, \quad \underline{\psi}_R = L_M\,(\underline{i}_s + \underline{i}_R) \tag{7}$$

respectively, where L_M is the magnetizing inductance and L'_s the stator transient inductance.

The electromagnetic torque is given by

$$T_e = \frac{3}{2} p\,\mathrm{Im}\left\{\underline{i}_s \underline{\psi}^*_R\right\} \tag{8}$$

where p is the number of pole pairs and the symbol * marks the complex conjugate. The equation of motion is

$$\frac{J}{p}\frac{\mathrm{d}\omega_m}{\mathrm{d}t} = T_e - T_L - b\frac{\omega_m}{p} \tag{9}$$

where J is the total moment of inertia of the mechanical system, T_L the load torque, and b the viscous friction coefficient.

The power into the stator can be expressed as

$$p_s = \frac{3}{2}\,\mathrm{Re}\{\underline{u}_s \underline{i}^*_s\} = p_{Cu} + p_f + p_m \tag{10}$$

where the resistive losses and the rate of change of the magnetic energy are

$$p_{Cu} = \frac{3}{2}\left(R_s i_s^2 + R_R i_R^2\right) \tag{11}$$

$$p_f = \frac{3}{2}\left(\frac{L'_s}{2}\frac{\mathrm{d}i_s^2}{\mathrm{d}t} + \frac{1}{2L_M}\frac{\mathrm{d}\psi_R^2}{\mathrm{d}t}\right) \tag{12}$$

respectively. The magnitude of the stator current is $i_s = |\underline{i}_s|$, and the magnitudes of other space vectors are denoted similarly. The mechanical power is

$$p_m = T_e\frac{\omega_m}{p} = \frac{J}{2p^2}\frac{\mathrm{d}\omega_m^2}{\mathrm{d}t} + T_L\frac{\omega_m}{p} + b\frac{\omega_m^2}{p^2} \tag{13}$$

where the last form is obtained using (9). The losses in the inverter will be omitted for simplicity, i.e. $p_s = p_d$ holds. Consequently, the current at the input of the inverter can be calculated as $i_d = p_s/u_d$.

III. DC-Link Dimensioning

Assuming continuous current i_{di} and considering the voltage u_{di} and the current i_d as input variables in (4), the undamped natural frequency and the damping ratio

$$\omega_n = \frac{1}{\sqrt{L_d C_d}}, \quad \zeta = \frac{1}{2\omega_n}\frac{R_d}{L_d} \tag{14}$$

are obtained, respectively. Conventionally, the DC link is dimensioned to effectively filter the six-fold mains frequency appearing in the voltage u_{di}. Hence, the natural frequency $\omega_n < 6\omega_g$ is selected, while the vicinity of $2\omega_g$ is avoided due to possibly unsymmetrical mains voltages.

The costs of the DC link can be significantly decreased if its natural frequency can be selected considerably higher than the six-fold mains frequency. To avoid the propagation of the switching harmonics to the mains side, the natural frequency should be lower than the switching frequency. This principle (i.e. $6\omega_g < \omega_n < \omega_{sw}$) leads to the restrictions

$$\frac{1}{\omega_{sw}^2 L_{d,min}} < C_d < \frac{1}{(6\omega_g)^2 L_{d,max}} \tag{15}$$

where $L_{d,min}$ and $L_{d,max}$ are the expected minimum and maximum values of the inductance L_d, and ω_{sw} is the angular switching frequency. According to (3) and (14), the damping of the DC link is usually better if no additional chokes are used.

The allowable range for the inductance L_d can be evaluated using (15). For example, the capacitance $C_d = 24$ µF corresponds to $L_{d,min} = 43$ µH and $L_{d,max} = 11$ mH. In practice, it is reasonable to avoid the vicinity of ω_{sw}, $6\omega_g$, and $12\omega_g$, leading to the allowable range of 50 µH $< L_d <$ 2 mH. If (15) cannot be realized due to a large inductance L_d, an active stabilization of the DC-link voltage may be used [10].

IV. Data of Example Drives

The data of two induction motor drives (2.2 kW and 37 kW) used in simulations are given in Table I. The 2.2-kW drive was also used for laboratory experiments. In this drive, the built-in 8-mH DC choke of a commercial frequency converter was short-circuited, and the original electrolytic capacitors (235 µF

TABLE I
DATA OF MOTOR DRIVES

Rated values of motor		
Power (kW)	2.2	37
Speed (r/min)	1 436	1 480
Frequency f_{N} (Hz)	50	50
Line-to-line voltage U_{N} (V, rms)	400	400
Current I_{N} (A, rms)	5.0	68.2
Torque T_{N} (Nm)	14.6	239
Motor parameters		
Stator resistance R_{s} (Ω)	3.7	0.069
Rotor resistance R_{R} (Ω)	2.1	0.044
Stator transient inductance L'_{s} (mH)	21	2.3
Magnetizing inductance L_{M} (mH)	224	31.3
Total moment of inertia J (kgm^2)	0.0155	0.831
Viscous friction coefficient b (Nm·s)	0.0025	0.0341
Mains and DC link		
Mains frequency (Hz)	50	50
Nominal DC-link voltage u_{dN} (V)	540	540
Inductance L_{d} (μH)	235	235
Resistance R_{d} (Ω)	0.5	0.06
Capacitance C_{d} (μF)	24	72
Undamped natural frequency ω_{n} (rad/s)	$2\pi{\cdot}2120$	$2\pi{\cdot}1220$

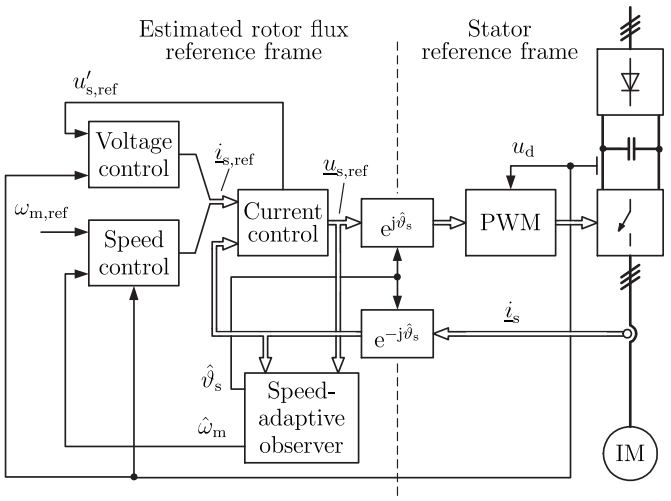

Fig. 2. Simplified block diagram of rotor-flux-oriented control system. Block "Speed control" includes speed controller augmented with DC-link overvoltage controller. Block "Voltage control" includes field-weakening and flux-braking controllers.

in total) were replaced with film capacitors (24 μF in total). The experimental setup was fed by a 500-kVA, 20-kV/400-V, 50-Hz distribution transformer. The unknown parameters R_{d} and L_{d} (needed only for simulations) were determined by fitting the simulated mains current to the measured one. The natural frequency depends on the inductance L_{d} while the damping is determined by the resistance R_{d}.

For the 37-kW drive, the capacitance of 72 μF was used in the simulations. The inductance L_{d} was chosen to equal that of the 2.2-kW drive since the same distribution transformer was assumed for both drives. The resistance R_{d} was calculated from (3), where the mains resistance $R_{\mathrm{g}} = 0$ and the resistance R'_{d} inversely proportional to the rated power of the drive were assumed. The total moment of inertia J for both drives was 2.2 times the inertia of the induction motor rotor.

V. SPEED-SENSORLESS CONTROL SYSTEM

A speed-sensorless rotor-flux-oriented control system proposed in [7] is used with minor modifications relating to the small DC-link capacitance. A simplified block diagram of the system is shown in Fig. 2. The parts essential to the small DC-link capacitance will be described here.

A. Sampling and Pulse-Width Modulation

A conventional space-vector pulse-width modulator and synchronized sampling (once per carrier period) are used in the simulations and experiments. The switching frequency is 5 kHz, i.e., $\omega_{\mathrm{sw}} = 100\omega_{\mathrm{g}}$. The duty cycles are determined in the beginning of the carrier period using the DC-link voltage u_{d} measured in the beginning of the previous carrier period. Even though the effects of the pulsating u_{d} can be partly compensated, the sampling delay and the change of u_{d} during the carrier period cause some errors in the produced stator voltage $\underline{u}_{\mathrm{s}}$.

The sampling delay could be decreased by sampling once per carrier half-period. The accuracy of the stator voltage could be further improved by measuring u_{d} several times per carrier half-period and by determining the switching instants on line during the carrier half-period [5]. This kind of modulation method is most advantageous if the per-unit DC-link capacitance is very small.

B. Flux Observer

The rotor flux estimate (whose amplitude is denoted by $\hat{\psi}_{\mathrm{R}}$ and angle by $\hat{\vartheta}_{\mathrm{s}}$) and the rotor speed estimate $\hat{\omega}_{\mathrm{m}}$ are obtained using a speed-adaptive flux observer [11]. Both the measured stator current $\underline{i}_{\mathrm{s}}$ and the stator voltage reference $\underline{u}_{\mathrm{s,ref}}$ are fed back to the flux observer. A pulse-width modulator cannot perfectly compensate the effects of the oscillating DC-link voltage on the voltage $\underline{u}_{\mathrm{s}}$, leading to noise in the stator current. Furthermore, a current controller migrates noise at lower frequencies to the voltage reference $\underline{u}_{\mathrm{s,ref}}$. Consequently, when a small DC-link capacitance is used, the damping of the flux observer is more important than usually due to the increased noise content. The damping of the observer can be analyzed using the corresponding linearized model.

C. Restriction of Dynamics

Contrary to the conventional DC link, overvoltages may be caused in the DC link by changes of the energy stored in the motor inductances or in the mains inductances. Usually, the larger the rated power of the drive, the smaller is the per-unit capacitance corresponding to (15). Hence, the rate of change of the stator current may have to be restricted to avoid DC-link overvoltages during transients, for example, by decreasing the bandwidth of the current controller. Furthermore, the ripple in the DC-link voltage is increased due to the smaller per-unit capacitance in larger-power drives.

Here, the current controller bandwidth of 6 p.u. is used for the 2.2-kW drive (being a typical value also for conventional drives), while the smaller bandwidth of 4 p.u. is needed for the 37-kW drive. The base values are defined in the Appendix. The bandwidth of the PI speed controller—including the active

damping [6]—is 0.15 p.u. for the 2.2-kW drive and 0.08 p.u. for the 37-kW drive.

D. Field Weakening

Field weakening is conventionally achieved by decreasing the flux reference inversely proportionally to the rotor speed. To guarantee the control of the stator current, some voltage margin is usually provided, leading to a reduction in the available maximum torque.

Even though the small DC-link capacitance does not ideally cause loss of the maximum available fundamental voltage [4], the voltage margin is worth minimizing in practice. Hence, the stator voltage is forced to its maximum value by adjusting the reference $i_{\mathrm{sd,ref}}$ of the flux-producing current component as [6]

$$\frac{\mathrm{d}i_{\mathrm{sd,ref}}}{\mathrm{d}t} = \gamma_{\mathrm{f}}\left[u_{\mathrm{s,max}}^2 - (u'_{\mathrm{s,ref}})^2\right], \quad -i_{\mathrm{s,max}} \le i_{\mathrm{sd,ref}} \le i_{\mathrm{sdN}} \tag{16}$$

where $\gamma_{\mathrm{f}} = 3R_{\mathrm{R}}\hat{\psi}_{\mathrm{R}}/(L'_{\mathrm{s}}u_{\mathrm{dN}})^2$ is the controller gain, $u'_{\mathrm{s,ref}}$ the magnitude of the unlimited voltage reference from the current controller, $u_{\mathrm{s,max}} = u_{\mathrm{d}}/\sqrt{3}$ the maximum stator voltage, $i_{\mathrm{s,max}}$ the maximum stator current, and i_{sdN} the rated value of the flux-producing current component.[1]

E. Braking Scheme

The speed controller is augmented with a DC-link overvoltage controller, limiting the braking torque based on the measured DC-link voltage and the maximum DC-link voltage $u_{\mathrm{d,max}}$. According to [7], the DC-link overvoltage controller is implemented as a dynamic limit for the torque-producing current component,

$$i_{\mathrm{sq,max}} = \frac{2}{3\hat{\psi}_{\mathrm{R}}\hat{\omega}_{\mathrm{m}}}\left[\frac{\alpha_{\mathrm{u}}C_{\mathrm{d}}}{2}\left(u_{\mathrm{d,max}}^2 - u_{\mathrm{d}}^2\right) + \hat{p}_{\mathrm{Cu}}\right] \tag{17}$$

where $\hat{p}_{\mathrm{Cu}} = (3/2)(R_{\mathrm{s}}i_{\mathrm{s}}^2 + R_{\mathrm{R}}i_{\mathrm{sq}}^2)$ is the estimate of the resistive losses. Ideally, the feedback (17) results in the closed-loop system $\mathrm{d}u_{\mathrm{d}}^2/\mathrm{d}t = \alpha_{\mathrm{u}}(u_{\mathrm{d,max}}^2 - u_{\mathrm{d}}^2)$ having the bandwidth α_{u}. The limit (17) is enabled if $\hat{\omega}_{\mathrm{m}}i_{\mathrm{sq,ref}} < 0$. Naturally, the limits corresponding to the maximum stator current and the breakdown torque are also used. Here, the bandwidth $\alpha_{\mathrm{u}} =$ 0.6 p.u., the maximum DC-link voltage $u_{\mathrm{d,max}} = 1.15 \cdot u_{\mathrm{dN}}$, and the maximum stator current $i_{\mathrm{s,max}} = 1.5$ p.u. are selected.

A flux-braking controller—making the losses larger during braking by increasing the flux-producing current component—is integrated with the field-weakening controller [7]. Based on (10) and (13), steady-state operation without a braking resistor is possible if the condition $T_{\mathrm{L}}\omega_{\mathrm{m}}/p + b\omega_{\mathrm{m}}^2/p^2 + p_{\mathrm{Cu}} \ge 0$ holds (where iron losses have not been taken into account). The flux braking is beneficial mostly in low-power drives due to their large per-unit losses. Furthermore, the flux braking has no effect in the field-weakening range due to the limited voltage.

If braking is frequently needed or the moment of inertia is high, causing long braking times, a braking resistor should be used to avoid an excessive temperature rise in the motor. If the braking time is not important, the flux-braking can be disabled while only the DC-link overvoltage controller is enabled.

[1]The gain γ_{f} equals the gain proposed in [6] approximately, but is simpler to implement. The limitation of $i_{\mathrm{sd,ref}}$ is modified in order to achieve faster dynamics during accelerations.

VI. Simulation Results

A. Harmonic Spectra

Simulated steady-state waveforms and their harmonic spectra are presented in this subsection. The drive operates at one per-unit speed under rated load torque. The results for the 2.2-kW and 37-kW drives are shown in Figs. 3 and 4, respectively.

The mains current of the 2.2-kW drive is shown in Fig. 3(a). The current has the total harmonic distortion (THD) of 40 %, where the harmonics up to the order 40 are taken into account in accordance with [12], [13]. For comparison, the corresponding THD for the drive with the original DC link is 44 %. Hence, the harmonic performance is slightly better than that of the conventional drive. The mains current of the 37-kW drive depicted in Fig. 4(a) has the THD of 31 %.

Figs. 3(b) and 4(b) show the DC-link voltage u_{d}. The sixth harmonic of the voltage u_{d} approximately equals that of the voltage u_{di} given in (2), while harmonics close to the natural frequency of the DC link ($\omega_{\mathrm{n}} = 42.4 \cdot \omega_{\mathrm{g}}$) are pronounced, and harmonics originating from the inverter switching can also be seen. The frequency response from u_{di} to u_{d} can be easily derived from (4). The harmonics in u_{d} originating from the mains side approximated using this frequency response and (2) correspond well to the simulated results in Figs. 3(b) and 4(b). The harmonics in the current i_{di} can be approximated similarly.

The waveform and the spectrum of the current i_{d} at the input of the inverter are presented in Fig. 3(c). Contrary to the corresponding spectrum of the conventionally dimensioned drive, the harmonic at $6\omega_{\mathrm{g}}$ and its multiples originating from the mains are clearly visible. No significant harmonics appear in the vicinity of the natural frequency.

Fig. 3(d) shows the waveform and the spectrum of the stator phase voltage u_{sa}. The harmonic components in the vicinity of $5\omega_{\mathrm{g}}$ and $7\omega_{\mathrm{g}}$ originate from the pulsating DC-link voltage and are larger than the corresponding components in the conventionally dimensioned drive.

B. Transients

Fig. 5(a) shows simulation results of an acceleration and a speed reversal for the 2.2-kW drive. The speed reference is stepped from zero to 1 p.u. at $t = 0.25$ s and reversed at $t =$ 1.25 s. The rated load torque is applied stepwise at $t = 0.5$ s and removed at $t = 1$ s. The removal of the load torque and the speed reversal activate the braking scheme. During the braking operation, the DC-link overvoltage controller drives the power p_{d} to zero while the flux-braking controller increases the losses by maximizing first the stator voltage at higher speeds and then the stator current at lower speeds. The performance of the drive is similar to the drive equipped with the conventional DC link, with the exception of slightly larger torque ripple at six times the mains frequency.

Fig. 5(b) presents simulation results of an acceleration, the negative rated load torque step and its removal, and a speed

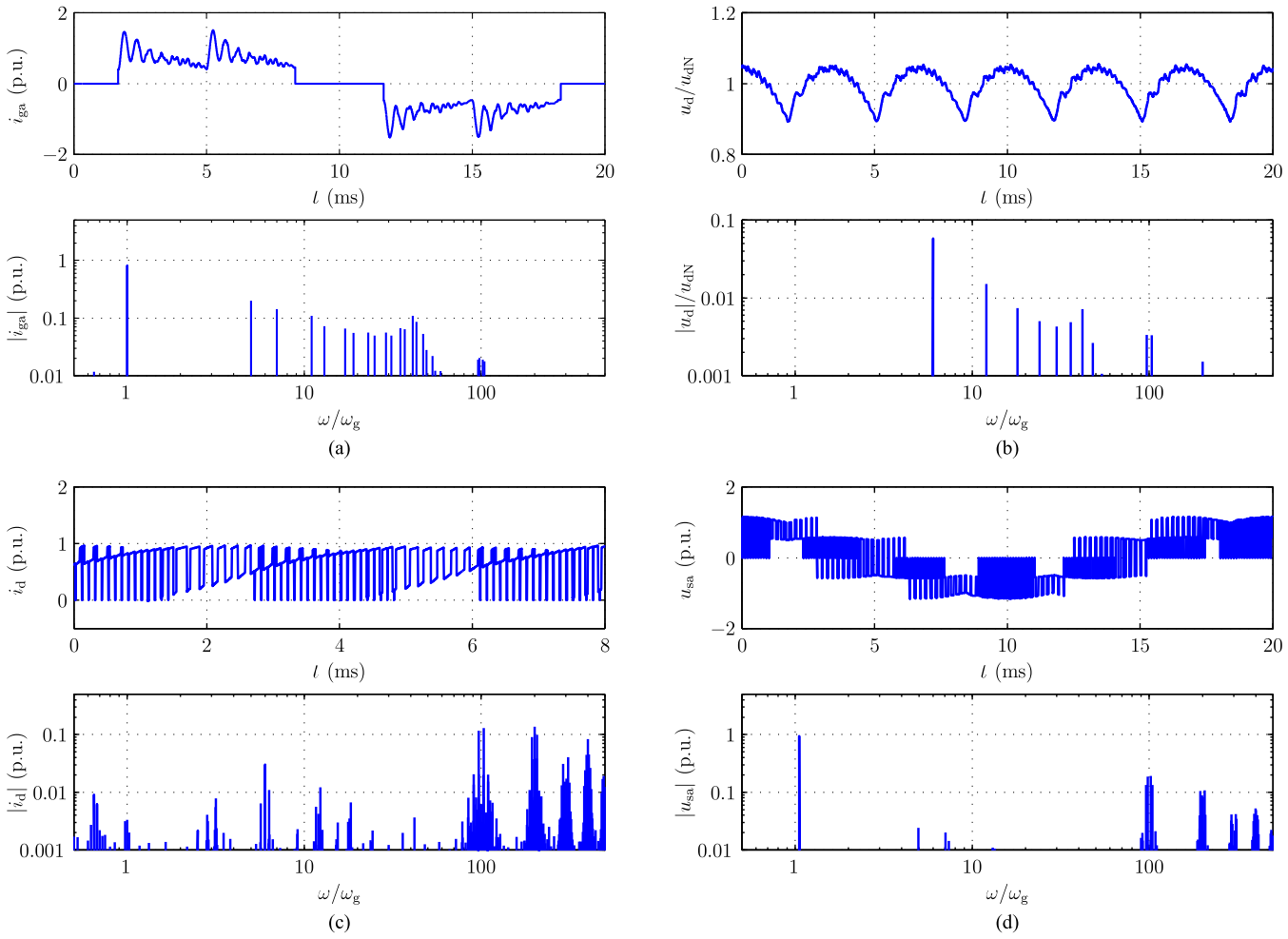

Fig. 3. Simulated waveforms and harmonic spectra for 2.2-kW drive at one per-unit speed and rated torque: (a) mains current i_{ga}; (b) DC-link voltage u_d; (c) current i_d at input of inverter; (d) stator phase voltage u_{sa}.

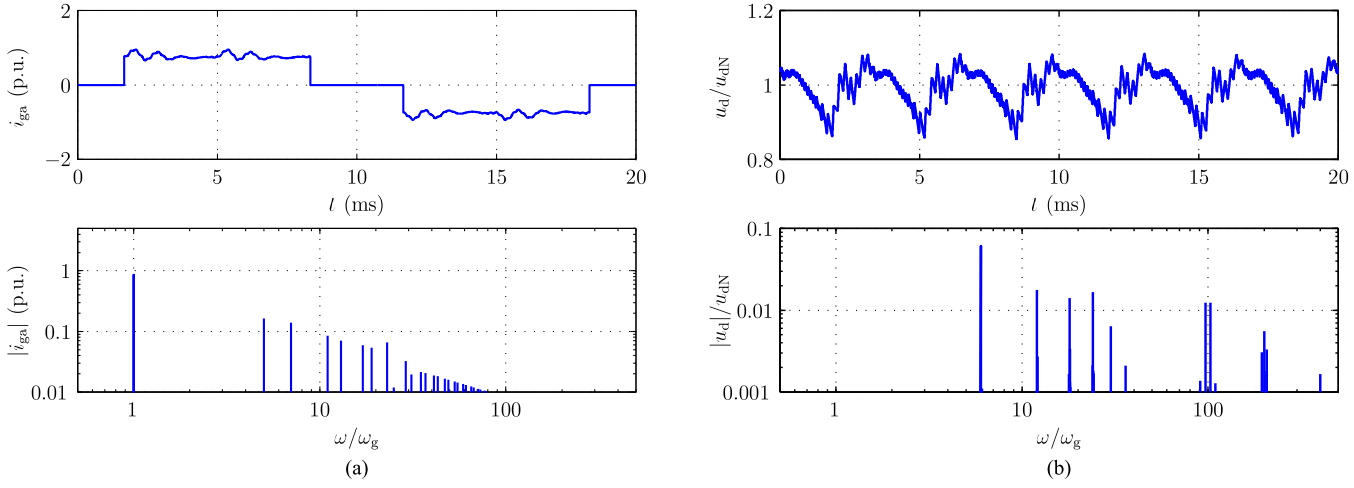

Fig. 4. Simulated waveforms and harmonic spectra for 37-kW drive at one per-unit speed and rated torque: (a) mains current i_{ga}; (b) DC-link voltage u_d.

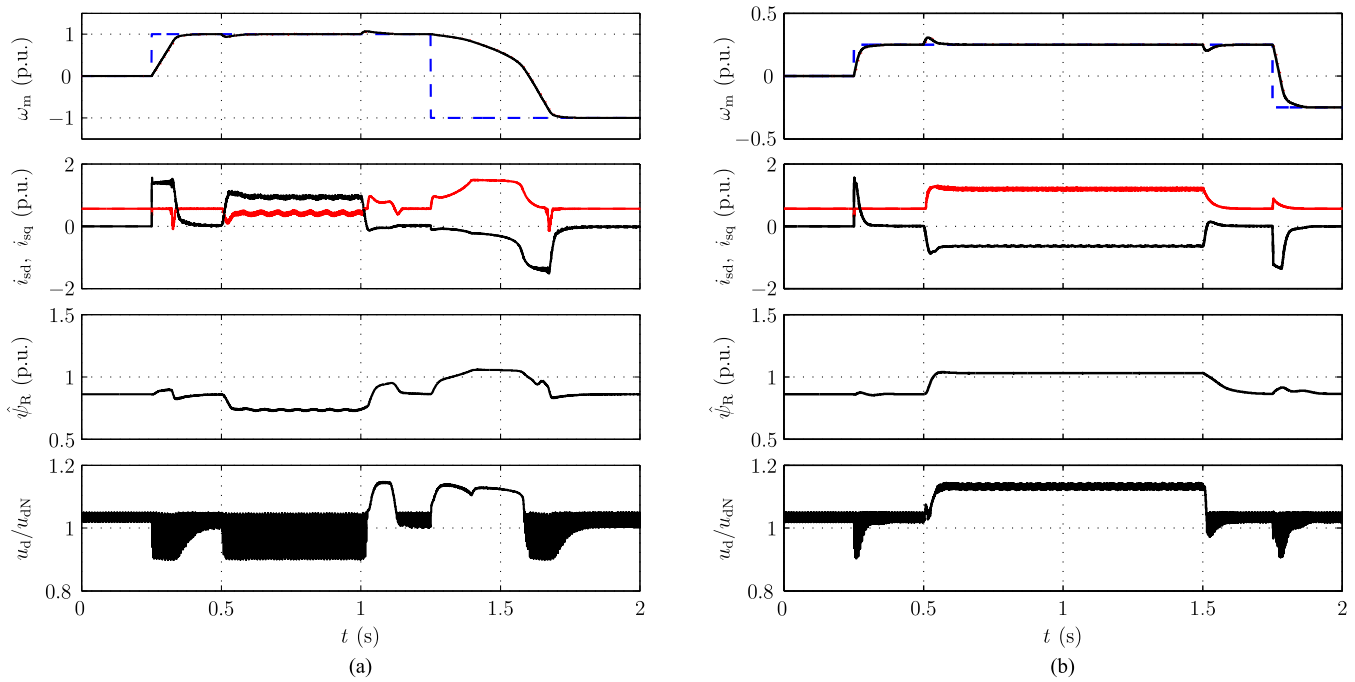

Fig. 5. Simulation results of 2.2-kW drive: (a) acceleration, load torque step, and speed reversal; (b) acceleration, negative load torque step, and speed reversal. First subplot shows measured speed (solid), estimated speed (dotted), and speed reference (dashed). Second subplot shows d and q components of measured stator current (solid) and their references (dashed) in estimated rotor flux reference frame. Third subplot depicts estimated rotor flux magnitude, and last subplot presents DC-link voltage.

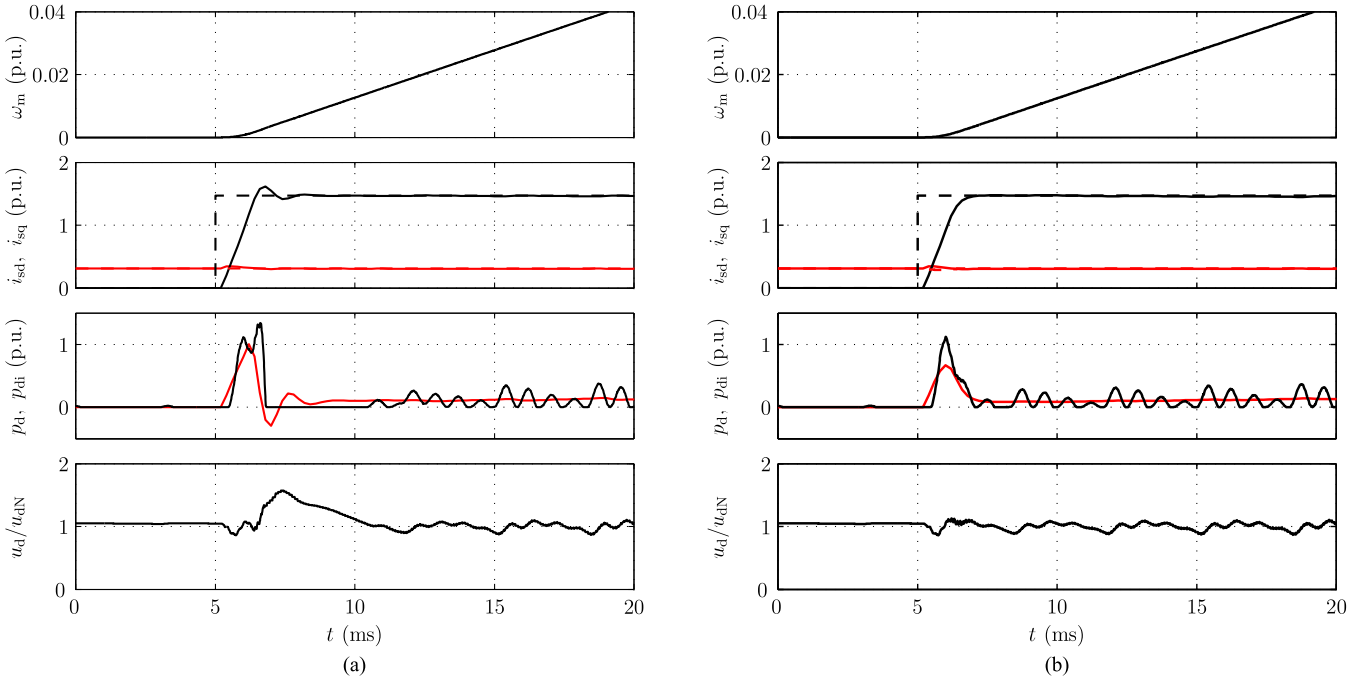

Fig. 6. Simulation results of 37-kW drive showing the beginning of acceleration when current controller bandwidth is (a) 8 p.u. and (b) 4 p.u. First subplot shows measured speed. Second subplot shows d and q components of measured stator current (solid) and their references (dashed) in estimated rotor flux reference frame. Third subplot shows power p_{di} (higher peak) and power p_d. Last subplot shows DC-link voltage. For clarity, power p_d and current components are averaged over one switching period.

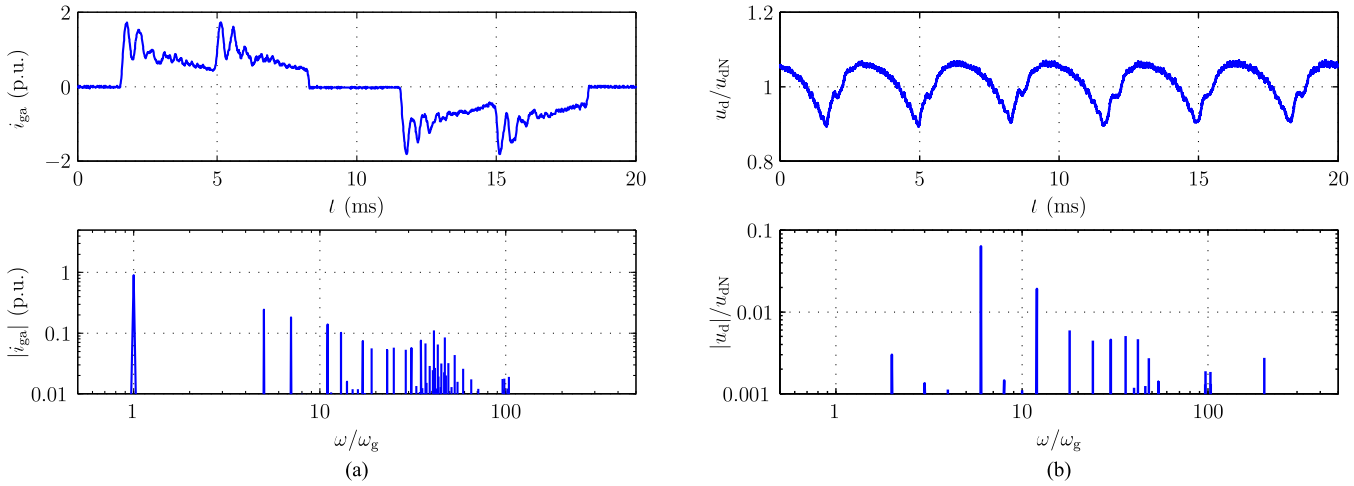

Fig. 7. Measured waveforms and harmonic spectra for 2.2-kW drive at one per-unit speed and rated torque: (a) mains current i_{ga}; (b) DC-link voltage u_{d}.

reversal for the 2.2-kW drive. The speed reference is stepped from zero to 0.25 p.u. at $t = 0.25$ s and reversed at $t = 1.75$ s. The negative rated load torque is applied stepwise at $t = 0.5$ s—causing the flux-braking controller to increase the flux-producing current component—and removed at $t = 1.5$ s. The negative rated load torque could not be achieved at speeds much higher than 0.25 p.u. (without a braking resistor). When the flux braking was disabled, speeds above 0.12 p.u. were not possible under the negative rated load torque.

Simulation results of the 37-kW drive showing the beginning of an acceleration are depicted in Fig. 6. The bandwidth of the current controller is 8 p.u. in Fig. 6(a). The speed reference is stepped from zero to the rated speed at $t = 5$ ms, causing the step in the reference of the torque-producing current component i_{sq}. The power into the DC-link capacitance is the difference between the power p_{di} from the mains side and the power p_{d} into the inverter. The small capacitance can deliver the power p_{d} only a while after $t = 5$ ms. Then, the power p_{di} and the current i_{di} increase rapidly and become larger than the power p_{d} and the current i_{d}, respectively. When the DC-link voltage u_{d} begins to rise, the power p_{di} being more than 1 p.u. cannot decrease immediately due to the inductance L_{d}. Hence, the DC-link voltage rises to approximately $1.3 \cdot u_{\mathrm{dN}}$ before the power p_{di} reaches zero. After $p_{\mathrm{di}} = 0$, the DC-link voltage still rises due to $p_{\mathrm{d}} < 0$. This phenomenon is explained in the following.

During the current rise, the rotor speed is $\omega_{\mathrm{m}} \approx 0$ due to the moment of inertia, resulting in the mechanical power $p_{\mathrm{m}} \approx 0$. Furthermore, the magnitude of the rotor flux remains approximately constant. Hence, the power p_{d} can be approximated based on (10) as

$$p_{\mathrm{d}} \approx p_{\mathrm{Cu}} + \frac{3}{2}\frac{L'_{\mathrm{s}}}{2}\frac{\mathrm{d}i_{\mathrm{s}}^2}{\mathrm{d}t} \tag{18}$$

In Fig. 6(a), there is an overshoot in the actual current component i_{sq}. This overshoot is reduced by the current controller, leading to $\mathrm{d}i_{\mathrm{s}}^2/\mathrm{d}t < 0$ and further $p_{\mathrm{d}} < 0$.

The DC-link overvoltage controller is inactive in Fig. 6 since $\hat{\omega}_{\mathrm{m}} i_{\mathrm{sq,ref}} > 0$. A simple way to eliminate the DC-link overvoltage seen in Fig. 6(a) is to constraint the rate of change of the stator current by decreasing the bandwidth of the current controller. In Fig. 6(b), the current controller bandwidth is 4 p.u., and no DC-link overvoltage appears. In the case of the 2.2-kW drive, similar overvoltages do not occur due to the significantly larger per-unit capacitance C_{d}.

VII. Experimental Results

The operation of the 2.2-kW drive was also investigated experimentally. The induction motor was fed by a frequency converter controlled by a dSPACE DS1103 PPC/DSP board. A permanent-magnet servo motor was used as a loading machine.

A. Harmonic Spectra

Measured steady-state waveforms and their harmonic spectra are presented in Fig. 7. The drive operates at one per-unit speed under rated load torque. Fig. 7(a) depicts the measured mains current corresponding to the simulation results in Fig. 3(a). Fig. 7(b) shows the DC-link voltage u_{d} corresponding to the simulation results in Fig. 3(b). It can be seen that the agreement between the simulation and experimental results is good. A harmonic component at $2\omega_{\mathrm{g}}$ can be seen in Fig. 7(b), indicating asymmetry in the mains voltages.

B. Transients

Fig. 8(a) shows an acceleration and a speed reversal corresponding to the simulation results in Fig. 5(a). Braking is faster than that in Fig. 5(a), mainly because the iron losses were not modeled in the simulation. During flux braking, a non-detrimental oscillation at the two-fold stator frequency appears in the DC-link voltage. The oscillation was negligible in the experiments when a conventionally dimensioned DC-link capacitance was used or the flux braking was disabled (but the DC-link overvoltage controller was used). The oscillation in the DC link originates from the oscillating flux magnitude, that is caused by the asymmetric saturation characteristics of the stator.

Fig. 8(b) presents operation under the negative rated load torque corresponding to the simulation results in Fig. 5(b). The

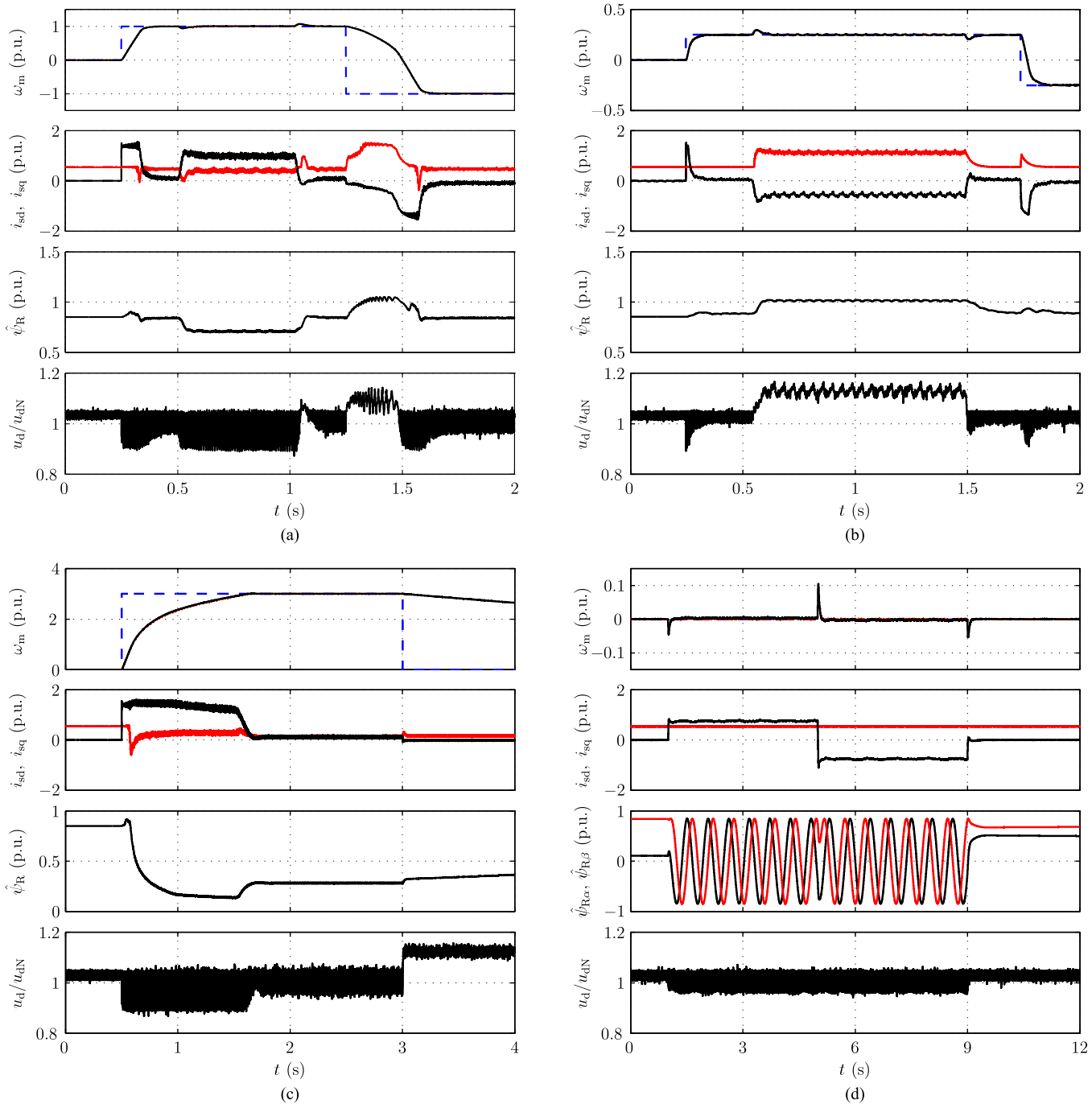

Fig. 8. Experimental results of 2.2-kW drive: (a) acceleration, load torque step, and speed reversal; (b) acceleration, negative load torque step, and speed reversal; (c) operation in field-weakening range; (d) rated load torque step and its reversal at zero speed reference. Explanations of curves are as in Fig. 5 except that components of estimated rotor flux in stator reference frame are shown in (d).

drive operates stably, even though an oscillation at the double stator frequency appears during flux braking.

Operation in the field-weakening range is depicted in Fig. 8(c). The speed reference is stepped from zero to 3 p.u. at $t = 0.5$ s and back to zero at $t = 3$ s. Since $i_{\mathrm{sd,ref}}$ is adjusted based on the available voltage, the current references are realizable in the field-weakening range. It can be seen that the DC-link overvoltage controller works well and no overshoots appear in the DC-link voltage. The flux-braking principle has no advantages in the field-weakening range since there is no voltage available for increasing the flux.

Fig. 8(d) depicts a load torque step and its reversal at zero speed reference. The rated load torque is stepwise applied at $t = 1$ s, reversed at $t = 5$ s, and removed at $t = 9$ s. Due to the minor stator power, the ripple in the DC-link voltage is lower than at high speeds.

VIII. Conclusion

A small DC-link capacitance can be used in vector-controlled induction motor drives when the natural frequency

of the DC link is chosen considerably higher than six times the mains frequency but lower than the switching frequency. No choke is needed at the input or output of the diode rectifier. Simulation and experimental results of a 2.2-kW drive equipped with a DC-link capacitance of 24 μF demonstrate that the drive can be operated in a wide speed and load range. The torque ripple is larger than that in the conventionally dimensioned drive but still within acceptable ranges. Based on simulation results, a small DC-link capacitance can also be used in a 37-kW drive, but the dynamics have to be restricted slightly.

APPENDIX
BASE VALUES

The nominal values are marked by the subscript N. They are given in Table I for the example drives. The base values are: angular frequency $\omega_{\mathrm{B}} = 2\pi f_{\mathrm{N}}$; voltage $u_{\mathrm{B}} = \sqrt{2/3}U_{\mathrm{N}}$; current $i_{\mathrm{B}} = \sqrt{2}I_{\mathrm{N}}$; impedance $Z_{\mathrm{B}} = u_{\mathrm{B}}/i_{\mathrm{B}}$; flux linkage $u_{\mathrm{B}}/\omega_{\mathrm{B}}$; power $(3/2)u_{\mathrm{B}}i_{\mathrm{B}}$; capacitance $1/(\omega_{\mathrm{B}}Z_{\mathrm{B}})$; and inductance $Z_{\mathrm{B}}/\omega_{\mathrm{B}}$.

ACKNOWLEDGMENT

The authors gratefully acknowledge the financial support given by ABB Oy and the contribution of Mr. P. Virolainen.

REFERENCES

[1] J. S. Kim and S. K. Sul, "New control scheme for AC-DC-AC converter without DC link electrolytic capacitor," in *Proc. IEEE PESC'93*, vol. 1, Seattle, WA, June 1993, pp. 300–306.

[2] L. Malesani, L. Rossetto, P. Tenti, and P. Tomasin, "AC/DC/AC PWM converter with reduced energy storage in the DC link," *IEEE Trans. Ind. Applicat.*, vol. 31, no. 2, pp. 287–292, Mar./Apr. 1995.

[3] Siemens Building Technologies Inc., "Harmonics White Paper," 2002. [Online]. Available: http://www.sbt.siemens.com/HVP/Components/Documentation/SI033WhitePaper.pdf

[4] H. Sarén, O. Pyrhönen, K. Rauma, and O. Laakkonen, "Overmodulation in voltage source inverter with small dc-link capacitor," in *Proc. IEEE PESC'05*, Recife, Brazil, June 2005.

[5] H. Sarén, O. Pyrhönen, J. Luukko, O. Laakkonen, and K. Rauma, "Verification of frequency converter with small dc-link capacitor," in *Proc. EPE'05*, Dresden, Germany, Sept. 2005.

[6] L. Harnefors, K. Pietiläinen, and L. Gertmar, "Torque-maximizing field-weakening control: design, analysis, and parameter selection," *IEEE Trans. Ind. Electron.*, vol. 48, no. 1, pp. 161–168, Feb. 2001.

[7] M. Hinkkanen and J. Luomi, "Braking scheme for vector-controlled induction motor drives equipped with diode rectifier without braking resistor," *IEEE Trans. Ind. Applicat.*, vol. 42, no. 5, pp. 1257–1263, Sept./Oct. 2006.

[8] P. C. Krause, O. Wasynczuk, and S. D. Sudhoff, *Analysis of Electric Machinery and Drive Systems*. Piscataway, NJ: IEEE Press, 2002.

[9] G. R. Slemon, "Modelling of induction machines for electric drives," *IEEE Trans. Ind. Applicat.*, vol. 25, no. 6, pp. 1126–1131, Nov./Dec. 1989.

[10] K.Pietiläinen, L. Harnefors, A. Petersson, and H.-P. Nee, "DC-link stabilization and voltage sag ride-through of inverter drives," *IEEE Trans. Ind. Electron.*, vol. 53, no. 4, pp. 1261–1268, June 2006.

[11] M. Hinkkanen, "Analysis and design of full-order flux observers for sensorless induction motors," *IEEE Trans. Ind. Electron.*, vol. 51, no. 5, pp. 1033–1040, Oct. 2004.

[12] *Adjustable Speed Electrical Power Drive Systems—Part 3: EMC Requirements and Specific Test Methods*, IEC Std. 61 800-3, Rev. 2004-08, 2004.

[13] *Electromagnetic Compatibility (EMC)—Part 3-12: Limits for Harmonic Currents Produced by Equipment Connected to Public Low-Voltage Systems with Input Current >16 A and ≤75 A per Phase*, IEC Std. 61 000-3-12, Rev. 2004-11, 2004.

Marko Hinkkanen (M'06) is currently an Acting Professor in the Department of Electrical and Communications Engineering, Helsinki University of Technology, Espoo, Finland. Since 2000, he has been with the Power Electronics Laboratory, Helsinki University of Technology. His research interests are in the areas of electric drives and electric machines. He received the M.Sc.(Eng.) and D.Sc.(Tech.) degrees from Helsinki University of Technology in 2000 and 2004, respectively.

Jorma Luomi (M'92) is a Professor in the Department of Electrical and Communications Engineering, Helsinki University of Technology, Espoo, Finland. He joined Helsinki University of Technology in 1980, and from 1991 to 1998 he was a Professor at Chalmers University of Technology. His research interests are in the areas of electric drives, electric machines, and numerical analysis of electromagnetic fields. He received the M.Sc.(Eng.) and D.Sc.(Tech.) degrees from Helsinki University of Technology, in 1977 and 1984, respectively.